Evaluation of Three-Dimensional Segmentation Algorithms for the Identification of Luminal and Medial–Adventitial Borders in Intravascular Ultrasound Images

Jon D. Klingensmith, Raj Shekhar, and D. Geoffrey Vince

Abstract—Intravascular ultrasound (IVUS) provides direct depiction of coronary artery anatomy, including plaque and vessel area, which is important in quantitative studies on the progression or regression of coronary artery disease. Traditionally, these studies have relied on manual evaluation, which is laborious, time consuming, and subject to large interobserver and intraobserver variability. A new technique, called active surface segmentation, alleviates these limitations and makes strides toward routine analyses. However, for three-dimensional (3-D) plaque assessment or 3-D reconstruction to become a clinical reality, methods must be developed which can analyze many images quickly. Presented is a comparison between two active surface techniques for three-dimensional segmentation of luminal and medial–adventitial borders. The force-acceleration technique and the neighborhood-search technique accurately detected both borders *in vivo* (r^2 = 0.95 and 0.99, Williams' index = 0.67 and 0.65, and r^2 = 0.95 and 0.99, WI = 0.67 and 0.70, respectively). However, the neighborhood-search technique was significantly faster and required less computation. Volume calculations for both techniques (r^2 = 0.99 and r^2 = 0.99) also agreed with a known-volume phantom. Active surface segmentation allows 3-D assessment of coronary morphology and further developments with this technology will provide clinical analysis tools.

Index Terms—Active contours, image segmentation, image sequence analysis, intravascular ultrasound.

I. INTRODUCTION

ANGIOGRAPHY has been the traditional method of assessing coronary artery disease for the past several decades. Contrast dye is injected into the coronary bloodstream and the heart is imaged with X-rays, producing a two-dimensional (2-D) projection of the complex three-dimensional (3-D) coronary artery tree. Only residual lumens can be visualized, and no information about the composition or thickness of the plaque or vessel wall is presented. These limitations can cause overestimation or underestimation of the degree of coronary obstruction or plaque burden, an important measure in studies of new coronary therapies and their effect on progression or regression of disease. In addition, it has been known that the risk of plaque rupture, the major cause of acute coronary events, is heavily dependent on the composition of the plaque and not the degree of stenosis alone [1]. Locating and treating all angina-causing lesions in the same manner does not ensure the best results, and the composition of the vessel wall is critical in selection of the proper therapeutic intervention. Although angiography provides little information about the structure or composition of the plaque or vessel wall, it remains the clinical gold standard for assessing coronary disease and is particularly useful in patients needing bypass surgery or angioplasty [2].

Intravascular ultrasound (IVUS) is a relatively new medical imaging technique which can provide information complementary to angiography. An ultrasound transducer on the tip of a catheter provides cross-sectional images of coronary arteries, clearly depicting the morphology of both plaque and arterial wall. Studies have documented the utility of IVUS in the quantitative assessment of the lumen, plaque, and vessel wall [3]–[5]. Other investigations have shown that IVUS can demonstrate disease in cases where angiography is misleading [6]–[9] and have confirmed the advantages of IVUS in assessing and selecting the proper coronary therapy [10]–[13]. The technology is not only useful in providing geometric information about the lumen, plaque, and vessel wall, it can also supply data regarding the specific components of the plaque [14], [15], an important parameter for the identification of lesions likely to rupture. Although it provides cross-sectional visualization of coronary anatomy, IVUS is limited by its tomographic nature. Three-dimensional information can equip clinicians with additional tools for visualization and diagnosis. These data are usually obtained by pull-backs, in which the catheter is moved through the artery while acquiring cross-sectional images along the length of the vessel. The difference between the medial–adventitial border (demarcating the boundary of the plaque-media complex with the surrounding adventitia) and the luminal border (demarcating the area of free lumen) defines the plaque area. Quantitative studies using IVUS require the identification of the luminal and medial–adventitial borders in these image sequences. Traditional methods of border detection involve manually tracing serial

IVUS images. This process is extremely tedious and time-consuming and data are difficult to reproduce, as interobserver and intraobserver variability can reach up to 20% [16]. In an attempt to improve the reproducibility and reliability in assessing small changes in the amount of coronary artery disease quantitatively, without the drawbacks of manual tracing, many automated and semi-automated segmentation techniques have been developed [16]–[20]. Segmenting borders manually in 3-D image sequences is laborious; therefore, automated or semi-automated techniques can reduce not only observer variability, but also the time needed for analysis. The development of 3-D segmentation techniques, taking advantage of the similarity of borders between frames, has been a recent evolution in the movement toward routine quantitative analysis in catheterization laboratories [21]–[28].

Three-dimensional IVUS yields more information than 2-D IVUS imaging alone in the visualization and assessment of coronary artery disease and the choice of intervention [29]. Techniques have been developed, facilitating more quantitative approaches, to make volumetric measurements using IVUS [22], [25], [30]–[35]. Straight reconstructions and 3-D morphometric analysis have been used successfully to evaluate the efficacy of stent deployment, rotational and directional atherectomy, and other interventions [36]–[42]. 3-D IVUS has also been used in studies of vascular remodeling, a phenomenon in which increases in plaque area cause an increase in vessel area. No luminal encroachment occurs, demonstrating a case where angiography would fail to identify coronary artery disease [43], [44]. These 3-D methods assume a straight vessel, ignoring the natural curvature of coronary arteries, which has been shown to have a nontrivial effect on vessel geometry produced by 3-D reconstructions [45], [46]. Spatially correct reconstructions, representing the geometry of the vessel accurately, could be useful clinically in assessing stent deployment and calculating true plaque volume. Fusing biplane angiography, which provides transducer pull-back path data, with IVUS, which provides vascular plaque and wall data, has spurred advances in 3-D reconstructions. Several methods have been developed to produce geometrically accurate 3-D vessels [47]–[52]. These techniques can also be used to observe remodeling [53], [54] and have unique potential for evaluation of intervention. An important requirement for any quantitative 3-D IVUS method is the accurate segmentation of luminal and medial–adventitial borders in pullback sequences.

Automated pullback devices, useful in providing longitudinal registration of IVUS slices, typically move the catheter 0.5 or 1.0 mm/s. The transducer rotates 1800 times/min, producing 30 images every second. At this frame rate, several hundred images will be acquired for a section of vessel only a few centimeters long. Although all 30 slices in each 1- or 0.5-mm section may not be needed to accurately reflect changes in the vessel wall [45], electrocardiogram (ECG) gated acquisition systems, which only acquire IVUS images at specified instances in the cardiac cycle, still generate hundreds of images for short to moderate-length segments [33]. The manual identification of vessel borders in even short segments, acquired with or without ECG gating, is impractical for online 3-D morphometric analysis or 3-D reconstruction. Online tools require fast and efficient segmentation methods, and it has been suggested that for useful clinical online tools, analysis must be completed in ≤ 10 min [40].

Our group has previously reported a high-level segmentation technique, subsequently referred to as the force-acceleration model, which utilizes the similarity between adjacent borders. A detailed description of this algorithm can be found in a recent article by Shekhar *et al.* [21]. It is robust to common problems in ultrasound image analysis, as the technique is based on the deformation of a surface template influenced by internal properties of the template and features in the image data. As intensity alone does not represent tissue type in ultrasound images, low level methods based only on gray-level intensity information are more susceptible to the limitations of IVUS imaging, such as intensity dropout, speckle, or low signal-to-noise ratio (SNR). Our approach, which has the advantage of utilizing low level constraints derived from the image data and high level constraints based on the size and shape of the structure of interest, successfully segments image sequences regardless of these limitations. The active surface technique described previously by our group is reliable and robust enough for IVUS segmentation [21], but is computationally expensive. Presented here is a new active surface algorithm referred to as the neighborhood-search model. Whereas the previous active surface technique utilized the discrete dynamic contour (DDC) model [55], extended to three dimensions, the new technique is based on the fast active contour (FAC) algorithm, a less expensive active contour algorithm [56], [57], and is also extended to three dimensions. The objective of this study was to compare the two active surface algorithms, and determine if the newer technique could produce results as accurate as the previously reported 3-D segmentation technique [21], but in less time.

II. ACTIVE SURFACE SEGMENTATION

Active contour, or "snakes," algorithms have become a useful solution for the problem of identifying and representing object contours and shapes in medical images. A model proposed by Kass *et al.* [58], which instigated the investigation and application of many variations of snakes algorithms [21], [55], [57]–[59], presented a method of contour definition in which the final contour could be influenced by higher level processes. This was a unique approach which differed from the traditional approach to object definition of edge detection and linking. In general, an active contour algorithm involves an initial contour, which is placed close to the desired image feature. This contour then deforms under external and internal forces until it converges on the object of interest. The internal forces maintain the continuity of the contour while the external forces are based on features in the image and serve to attract the contour to these features, typically edges. The model developed by Kass *et al.* [58] consisted of energy terms and a method for finding contours which minimized this energy function was presented. However, others have noted that the method of minimization to find the optimal contour solution has limitations, as it can be unstable, it will allow the contour vertices to bunch together at corners due to external (edge) forces, and the contour model may shrink due to internal forces. The DDC model of Lobregt and Viergever [55] and the FAC algorithm of Williams and Shah [57] both

addressed these issues, and each offered alternative solutions which utilize the advantages of active contour algorithms, but avoid the limitations of previous models.

In the earlier model created by Kass *et al.* [58], the energy function of a contour was defined as

$$E^*_{\text{snake}} = \int_0^1 E_{\text{int}}(\boldsymbol{v}(s)) + E_{\text{image}}(\boldsymbol{v}(s)) + E_{\text{con}}(\boldsymbol{v}(s))\,ds \tag{1}$$

where

E_{int} represents the internal energy of the spline contour due to bending,

E_{image} represents the image forces, and

E_{con} introduces external constraints.

The authors minimized this function using variational calculus to produce the desired resulting contour. Amini *et al.* [60] pointed out the instability of this method of minimization and the tendency for points to bunch on strong portions of edges. They developed a new minimization procedure for this function using dynamic programming, which had several advantages over variational calculus [60]. The points on the contour are moved within a discrete grid, as opposed to the method of Kass *et al.* [58] and the DDC method of Lobregt and Viergever [55], in which new vertex locations are calculated as real numbers. The minimization method described in [60] is also numerically stable. Although the dynamic programming minimization offered key advantages to the variational calculus approach, it has large memory requirements and is computationally expensive. Williams and Shah [57] introduced an algorithm, which is stable, flexible, calculates vertex locations within a discrete grid, and runs much faster than dynamic programming. This algorithm, on which our new 3-D technique is based, is described briefly below.

A. Two-Dimensional Fast Active Contour Model

The quantity being minimized in the FAC method is

$$E = \int (\alpha(s)E_{\text{cont}} + \beta(s)E_{\text{curv}} + \gamma(s)E_{\text{image}})\,ds. \tag{2}$$

The first term constrains the first-order continuity and the second term constrains second-order continuity. The first two terms relate to E_{int} from (1). The last term is based on some feature in the image (in this application, edge strength) and is the same as E_{image} in (1). The parameters α, β, and γ are weighting factors which control the relative influence between the terms.

Like the active contour algorithms before it, the FAC method is iterative. For each iteration through the contour vertices, a neighborhood of the vertex is searched and the location in the neighborhood with the minimum value for (2) is chosen as the new location for the vertex. The size of this neighborhood is defined by the user. This process is repeated until the number of vertices moved to new locations is less than a specified threshold or the user-defined maximum number of iterations has been reached.

If V_i is the current vertex for which the new location is being calculated, and the index i ranges from 1–N, where N is the number of vertices on the contour, E_{cont} in (2) is formulated by taking the average spacing (Euclidean distance) between all the contour vertices and subtracting the distance between the current vertex and the vertex before it. This is defined as

$$E_{\text{cont}} = d - \left| V_{i\bmod N} - V_{(i-1)\bmod N} \right| \tag{3}$$

where

d average distance between vertices;

V_i current vertex;

V_{i-1} vertex before it.

Using this expression eliminates the possibility of the curve shrinking and still satisfies first-order continuity by encouraging even spacing. Points with a distance between them which is near the average distance between all vertices will have small values for E_{cont}. The average distance between points is recalculated for every iteration.

The second term represents curvature. The continuity term in (3) encourages the points to remain evenly spaced, therefore, the following is used for the curvature term:

$$E_{\text{curv}} = \left| V_{(i-1)\bmod N} - 2V_{i\bmod N} + V_{(i+1)\bmod N} \right|^2 \tag{4}$$

where

V_i current vertex;

V_{i-1} previous vertex;

V_{i+1} next vertex.

Equation (4) gives a reasonable estimate of curvature and was the most computationally efficient of the curvature estimates tested earlier [57]. Small values of this expression encourage the reduction of curvature, which helps the contour maintain its shape and prevents the formation of corners. If corners or other shape features are desired in the final results, β can be adjusted accordingly to raise or lower the influence of curvature in the function minimization.

E_{image} is the force used to attract the contour to the desired image feature and is normally gradient magnitude. For this particular application, this force was formed in a specific manner, as described in preprocessing (Section II-C). For each neighborhood, the image force is calculated using

$$E_{\text{image}} = \frac{(\min - g)}{(\max - \min)} \tag{5}$$

where

$\max$ maximum gradient value in the neighborhood;

$\min$ minimum;

g gradient at the current location of the vertex.

The image energy term is more negative for large gradient values, so the vertices will be attracted to edges with strong energy.

Equations (3) and (4) are normalized to the range of 0–1 using the maximum value in the neighborhood. The third term is already normalized to this range, as shown in (5). These terms are each multiplied by their respective weighting factors and then added together, as shown in (2), to form the energy calculation for a specific contour location.

B. Placement of Initial Surface

The placement of the initial surface for the FAC-based active surface segmentation is performed in the same manner as the placement of the initial surface template for the DDC-based method. Initial contours must be placed on the first slice, last
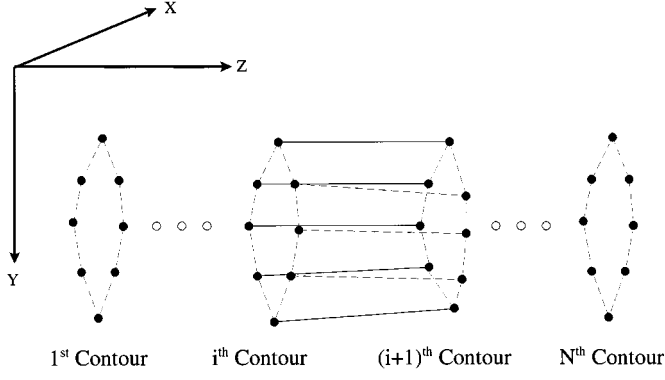
Fig. 1. The approximately cylindrical surface model generated from control points serves as the initial template for the active surface segmentation algorithms. Each contour is associated with an original image plane in the 3-D stack of images.

slice, and several intermediate slices, according to any significant deviations in shape and/or location of the desired borders between adjacent slices. The control points entered on one slice are linearly interpolated to generate a closed contour. Each contour has the same number of vertices, so a one-to-one relationship can be established among the vertices between contours. The contours are used to generate a surface template (Fig. 1), also by linear interpolation. Approximately one initial contour was required for every seven to ten slices from IVUS pullback sequences, and 10–12 points placed close to the desired border were needed to generate single contours.

C. Preprocessing

The desired feature of interest in IVUS images is a radial transition from dark to light which corresponds to the transition from lumen to intima for luminal borders or media to adventitia for the medial–adventitial border. If follows that the gradient used for the calculation of (5) should be formulated in a radial direction. The images were transformed into the polar domain, which is the native form in which IVUS data are acquired. Then the gradient calculation was performed on each scan line using the convolution kernel $\{-6, -4, -2, 0, 2, 4, 6\}$, which was determined empirically. The gradients were then converted back into Cartesian format using bilinear interpolation. Then, the gradient images were stacked to form the 3-D potential field used to calculate E_{image}. Fig. 2 shows examples of *in vivo* and *in vitro* images with their corresponding gradient images.

D. Deformation

Extending (2) for energy function minimization in a 3-D surface model yields

$$E = \int (E_{\text{cont}} + E_{\text{curv}} + \gamma(s)E_{\text{image}}) \, ds \qquad (6)$$

where E_{cont} and E_{curv} are now split into transverse and longitudinal components defined by

$$E_{\text{cont}} = \alpha_{\text{tran}}(s)E_{\text{cont, tran}} + \alpha_{\text{long}}(s)E_{\text{cont, long}} \qquad (7)$$

and

$$E_{\text{curv}} = \beta_{\text{tran}}(s)E_{\text{curv, tran}} + \beta_{\text{long}}(s)E_{\text{curv, long}}. \qquad (8)$$

The weighting factors α and β from (2) now also have transverse and longitudinal components, α_{tran} and α_{long}, and β_{tran}

and β_{long}. The tangential components of the external forces applied in the force-acceleration model do not make a significant contribution to the overall deformation; consequently, only the radial component is applied. A similar adjustment is made in the neighborhood-search active surface algorithm. The longitudinal term in E_{cont} is eliminated, yielding the new energy function

$$E = \int \begin{pmatrix} \alpha_{\text{tran}}(s)E_{\text{cont, tran}} + \beta_{\text{tran}}(s)E_{\text{curv, tran}} \\ + \beta_{\text{long}}(s)E_{\text{curv, long}} + \gamma(s)E_{\text{image}} \end{pmatrix} ds \qquad (9)$$

and the neighborhood searched for the new surface vertex location is restricted to the in-plane x–y locations. Vertices are not allowed to move from one plane (z coordinate) to another. The size of the neighborhood is defined by the user.

The transverse component of the continuity term $E_{\text{cont,tran}}$ in (9) is formulated in exactly the same way as the continuity term in the 2-D FAC algorithm, shown in (2). Because we are restricting the neighborhood to the x–y in-plane locations to limit the deformations to the radial direction, only the vertices on the same plane are used to calculate the average distance in the continuity term.

The two curvature terms in (9) help the surface maintain its overall shape and prevent it from forming kinks or sharp points. Before defining the longitudinal and transverse curvature terms, an important difference between active contour algorithms must be noted. The DDC model allows the number of vertices to change according to a resampling procedure dependent on the distance between vertices. However, the FAC algorithm begins with a fixed number of vertices whose locations are optimized according to (2). The same difference holds true for the 3-D active surface segmentation techniques based on these 2-D algorithms. Whereas the force-acceleration model allows the number of vertices on a contour to change, the neighborhood-search model begins with a fixed number of vertices on each contour, which is the same for all contours. As a result, the transverse curvature term is formulated as shown in (10). An index j, which ranges from zero to the number of contours on the surface, is added. It is defined as

$$E_{\text{curv, tran}} = \left| V_{j, (i-1) \bmod N} - 2V_{j, i \bmod N} + V_{j, (i+1) \bmod N} \right|^2 \qquad (10)$$

where N is the constant number of vertices on each contour. The longitudinal curvature term is given by

$$E_{\text{curv, long}} = \left| V_{j-1, k} - 2V_{j, i} + V_{j+1, l} \right|^2 \qquad (11)$$

where j refers to the contour on which the current vertex resides. The index i refers to the current vertex and k and l refer to the vertex on the contours before and after the current contour, respectively, that are closest to the current vertex (based on Euclidean distance). For the end contours, where $j - 1$ or $j + 1$ would be undefined, the x–y location of the current vertex is duplicated for the longitudinal neighbor which would otherwise be undefined.

For the neighborhood-search algorithm in 3-D, the E_{image} term was constructed based on the x–y plane neighborhood. For a neighborhood range of five pixels, only 25 energy computations were performed (instead of 125 for a potential 3-D neighborhood). This reduced the computational expense of the algorithm and limited the deformation to the local radial direction,
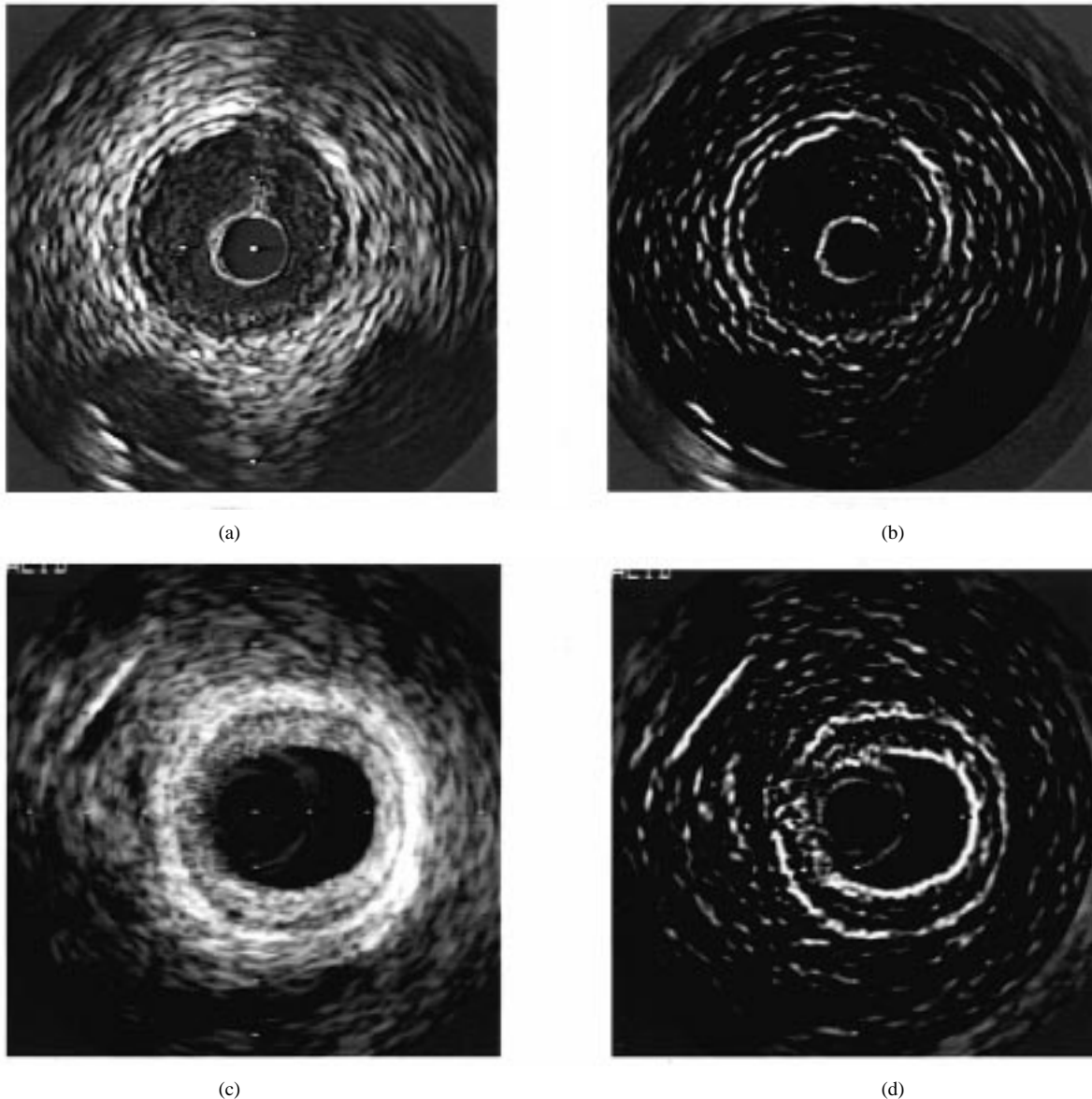
(a)

(b)

(c)

(d)

Fig. 2. Example images showing gradient calculations used for the neighborhood-search algorithm. (a) An *in vivo* image is shown (b) with its corresponding radial gradient image . Also shown is an *in vitro* example with (c) the original and (d) the gradient image.

i.e., the vertices could only be moved to a new neighboring location within the same x–y plane (see Fig. 3).

The continuity term and the longitudinal and transverse curvature terms are normalized to the range of zero to one using the maximum value in the neighborhood. The third term is also normalized to this range. These terms are each multiplied by their respective weighting factors and then added together to form the energy calculation for a specific contour location. Different levels of importance could be assigned to the different terms using the weighting factors α_{tran}, β_{tran}, β_{long}, and γ. For example, if a stiffer surface were desirable, α_{tran}, β_{tran}, and β_{long} would be set large compared to γ. However, if a less stiff snake, more attracted to image features, was desirable, γ would be set large with respect to the other factors. The different factors would generally be different for different applications. The active contour in 2-D snakes algorithms is analogous to a surface in 3-D snakes algorithms. Therefore, like the

iterations for the force-acceleration model, the iterations for the neighborhood-search technique were performed over the entire surface, i.e., the new locations for every vertex on the whole surface would be calculated and the vertices moved to new locations before the next iteration started. The algorithm stopped when either the number of vertices moved to new locations fell beneath a specified threshold for a given iteration or a maximum number of iterations was reached.

III. EXPERIMENTAL METHODS

IVUS images were acquired by digitizing S-VHS video tape with a video capture card (miroVideo DC30 Pro, Pinnacle Systems, Mountain View, CA) at a resolution of 640 × 480. The depth on the IVUS console was set to 5 mm for each pullback, and the calibration markers displayed on the digitized images were used to derive the pixel size of 0.03 mm (the resolution
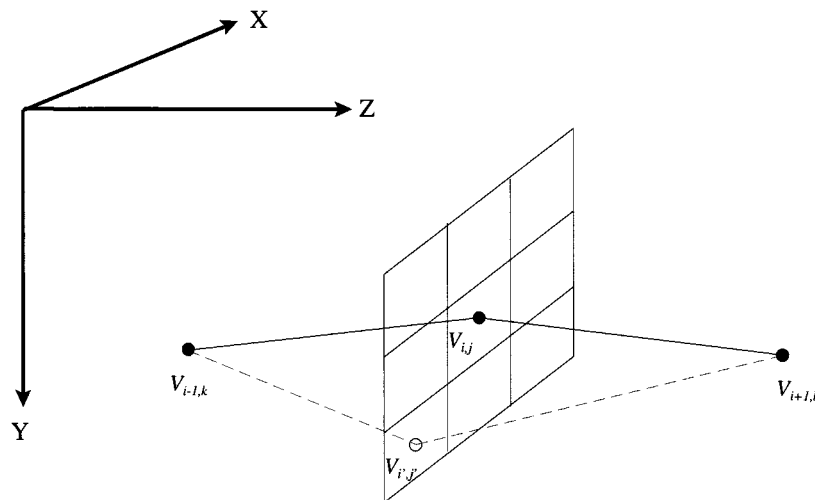
Fig. 3.   Depiction of the possible new locations of a vertex for the neighborhood-search algorithm for a 3 × 3 neighborhood.

of S-VHS video), which was used to calculate cross-sectional area and perimeter for the detected borders. The images were acquired using the JPEG standard at a rate of 30 frames/s and were later converted to uncompressed raw data for analysis.

Both active surface segmentation algorithms were implemented in the same graphical user interface (GUI), called IVUSLab, which runs on Windows NT. This allowed for convenient, user-friendly segmentation utilizing either active surface segmentation technique. For the algorithm testing, analysis was conducted with the IVUSLab software running on a Pentium II based 450-MHz PC.

A. Experimental Data

1) In Vivo Data: Three motorized pullbacks in coronary arteries, one left circumflex (LCX) artery and two left anterior descending (LAD) arteries, were performed with a 40 MHz Boston Scientific Discovery IVUS imaging catheter (Boston Scientific, San Jose, CA) using an automated pullback device set at 0.5 mm/s. Sixty seconds of images were digitized to sample a 30-mm segment of artery, yielding 1800 IVUS images. The image sequences were gated to end-diastole, resulting in a different number of slices for each 30-mm segment, depending on the heart rate of the patient (44 images, 64 images, and 77 images over 30 mm). There were 185 images total for *in vivo* validation.

2) In Vitro Data: Three human left anterior descending (LAD) coronary arteries with approximately 3 cm of surrounding tissue were obtained at autopsy by dissection from the aortic ostia to the apex of the ventricles. Vessels from subjects who had undergone previous interventional procedures or vessels that were totally occluded or so heavily diseased as to preclude introduction of the IVUS catheter were excluded.

The tissue was placed in a custom-engineered pressurization system and arranged to approximate its position *in situ*. The vessel was pressurized (100 mmHg) with phosphate-buffered saline to simulate physiological conditions. One pullback was performed in each of the explanted LADs with a 45-MHz Hewlett-Packard *Scout* IVUS imaging catheter (Hewlett-Packard, Andover, MA) using an automated pullback

device set at 1.0 mm/s. Two frames were sampled for each millimeter of artery yielding 60 image slices over a 30-mm segment at known spacing. This resulted in 180 images total for *in vitro* validation.

3) Known-Volume Phantom: To validate the ability of the algorithms to represent volumes, a clear acrylic phantom was constructed. The phantom contained cylindrical sections of 2- to 6-mm diameter sections. Each section was 1 cm long, providing known dimensions and a known volume for each cylindrical section. Three pullbacks were performed through the phantom with a 45 MHz Hewlett-Packard *Scout* IVUS catheter (Hewlett-Packard, Andover, MA) at 1 mm/s. Two frames/mm were segmented with both active surface techniques and the resulting cross-sectional areas were used to calculate the volume of each section. The calculated volumes were compared to the actual known volume of the cylinder.

B. Validation Statistics

The images from the *in vitro* and *in vivo* pullbacks were traced by four expert human observers. These same pullback images were segmented using both algorithms implemented in the IVUSLab 3-D segmentation software. The editing tool of the software was used by the operator to adjust the resulting luminal and medial–adventitial borders to the desired location, if necessary. Borders, both before and after user-editing, were saved for comparison. The borders from the semi-automated 3-D segmentation techniques and the manually traced borders were then used to calculate Williams' index (WI), a ratio of the average observer-observer variability to the average computer-observer variability [61]. A WI of 1.0 implies the computer measurement does not differ from the expert observers more than the expert observers differ among themselves. Any metric can be used for the WI calculation, and for this validation, cross-sectional area, perimeter, Hausdorff distance, and average distance were each used to compute WI. Hausdorff distance is defined as the maximum of the smallest distances between the points on two curves [61], [62], and the average distance was the average of radial disagreement between two contours.
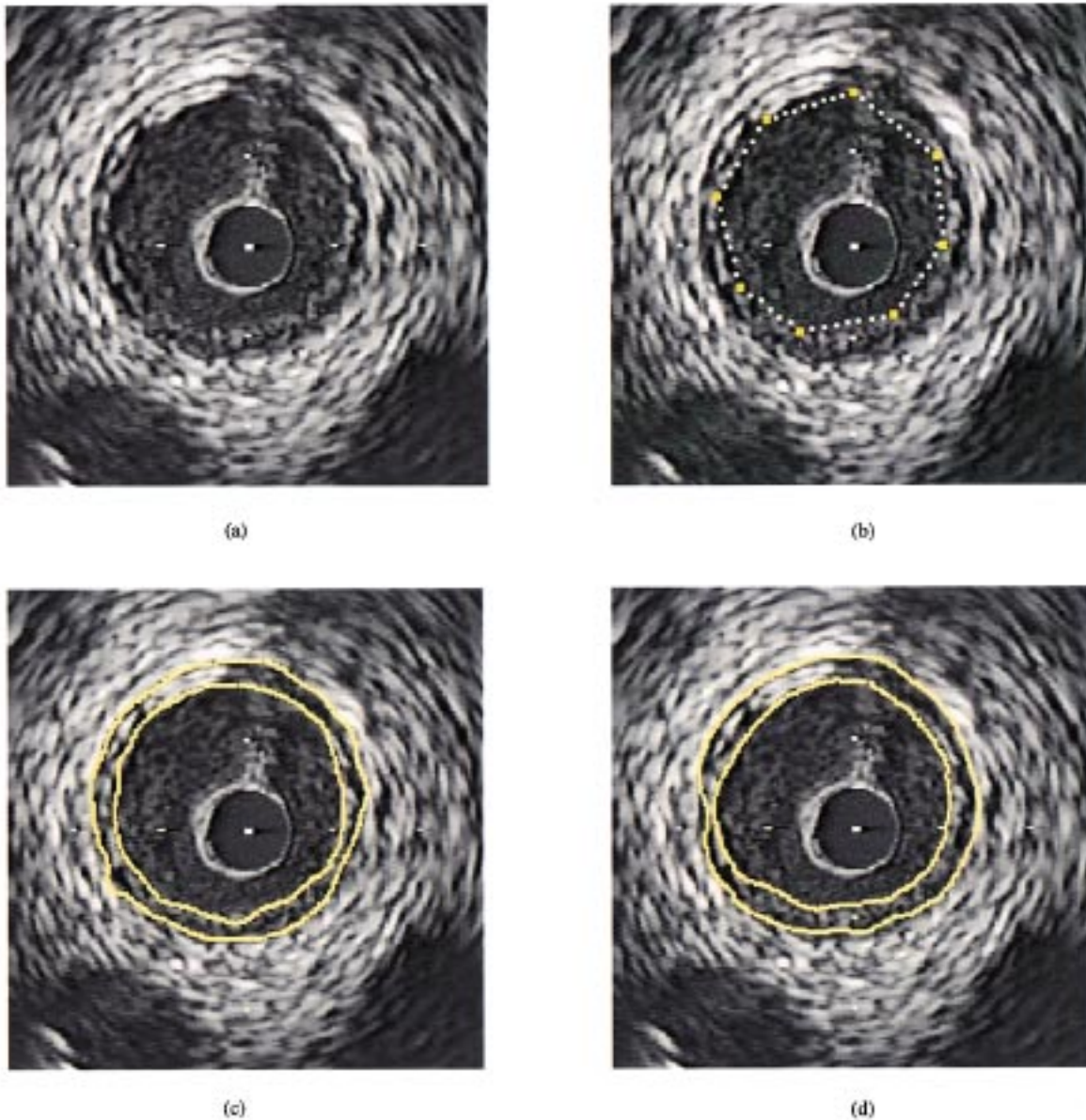
Fig. 4. Example of *in vivo* luminal and medial–adventitial border detection with (a) the original image, (b) the image with the initial contour shown, (c) borders as detected by the force-acceleration algorithm, and (d) borders as detected by the neighborhood-search algorithm.

Linear regression analysis was also used to validate the semi-automated segmentation techniques. Correlation coefficients (r^2), slope, and y intercept was calculated to compare the cross-sectional areas and perimeters from the automated technique and the average of the expert observers. To compare the volumes calculated by the segmentation, regression analysis was again employed. r^2, as well as the slope and y intercept, were calculated to compare the actual volumes of the phantom sections to the volumes computed from the segmentation results.

C. Algorithm Timing

To eliminate any effects of implementation overhead when comparing algorithm timing, central processing unit (CPU) time required for each algorithm was recorded using function profiling. In this manner, direct comparisons could be made on the computational efficiency of the techniques. A pullback with 60 images was used as test data, and each algorithm was profiled three times. The average CPU times for preprocessing and snake deformation were recorded for comparison.

IV. RESULTS

Overall, both the force-acceleration 3-D technique and the neighborhood-search 3-D technique successfully segmented IVUS images. Good correlations were found for cross-sectional area and perimeter comparisons between both automated techniques and the average from the expert human observers. A sample *in vivo* image with detected luminal and medial–adventitial borders from both techniques is shown in Fig. 4 and a sample *in vitro* image with detected borders is shown in Fig. 5.

A. Algorithm Accuracy

Correlation coefficients calculated using cross-sectional area and perimeter measurements for both algorithms are shown in
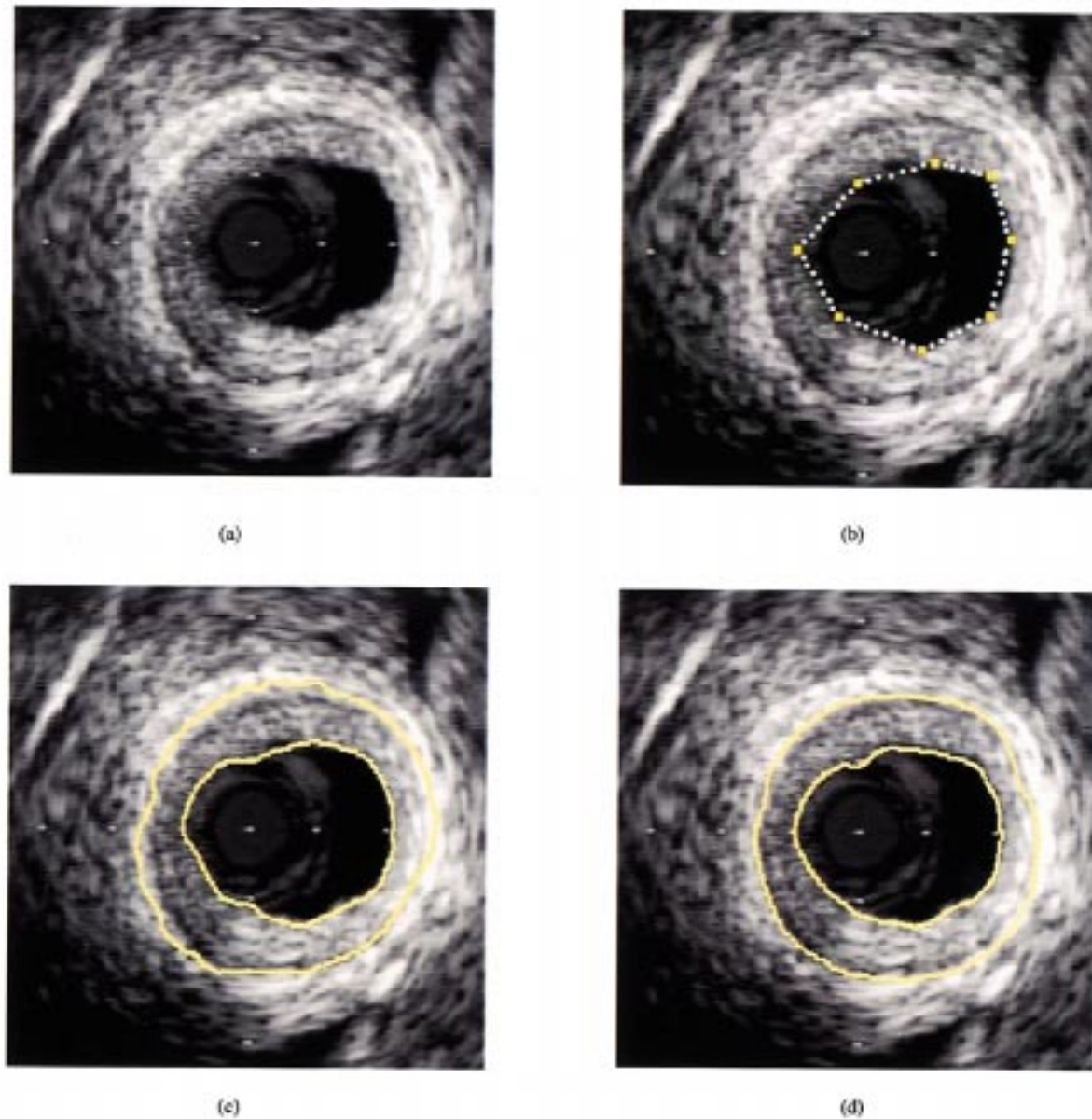
Fig. 5. Example of *in vitro* luminal and medial–adventitial border detection with (a) the original image, (b) the image with the initial contour shown, (c) borders as detected by the force-acceleration algorithm, and (d) borders as detected by the neighborhood-search algorithm.

Table I. r^2 values for detected luminal and medial–adventitial borders are shown. Preedit and postedit values for *in vivo* and *in vitro* data sets are presented.

Table II contains the WI values calculated for *in vivo* luminal border detection by both 3-D algorithms. The 95% confidence intervals, computed using a jack-knife resampling procedure, are also presented. The WI value is the ratio of average observer–observer variability to the average computer–observer variability; if 1.0 falls within the confidence interval, then it is concluded that the computer observation varies from the expert observers no more than the observers vary among themselves. The preedit and postedit WI values for each algorithm based on each of the four metrics used, cross-sectional area, perimeter, average distance, and Hausdorff distance, are presented.

The WI values calculated for *in vivo* medial–adventitial border detection are shown in Table III, which also contains both preedit and postedit values for comparison. Tables IV and V compare the accuracy of the two algorithms in detecting both luminal and medial–adventitial borders, respectively, in the *in vitro* data set.

B. Editing

An important question for semi-automated medical image analysis is if user correction of the borders makes a statistically significant improvement on segmentation results. For the problem at hand, we can compare the preedit borders and the validation statistics generated by these borders to the post- edit

TABLE I
R^2 VALUES FOR *In Vivo* LUMINAL BORDER DETECTION BEFORE USER CORRECTION

Borders (3 patients, 185 images)	Correlation Coefficient Values (R^2)							
	Force-Acceleration Algorithm				Neighborhood-Search Algorithm			
	Area		Perimeter		Area		Perimeter	
	Pre-edit	Post-edit	Pre-edit	Post-edit	Pre-edit	Post-edit	Pre-edit	Post-edit
In vivo Luminal Border Detection	0.95	0.95	0.92	0.93	0.95	0.94	0.88	0.88
In vivo Medial-Adventitial Border Detection	0.99	0.99	0.97	0.98	0.99	0.99	0.98	0.98
In vitro Luminal Border Detection	0.93	0.95	0.87	0.89	0.95	0.96	0.87	0.90
In vitro Medial-Adventitial Border Detection	0.94	0.96	0.81	0.82	0.95	0.97	0.91	0.94

TABLE II
WI VALUES FOR *In Vivo* LUMINAL BORDER DETECTION

Parameters (3 patients, 185 images)	WI (95% Confidence intervals)			
	Force-Acceleration Algorithm		Neighborhood-Search Algorithm	
	Pre-edit	Post-edit	Pre-edit	Post-edit
Area	0.75 (0.47, 1.02)	0.88 (0.78, 0.97)	0.60 (0.32, 0.95)	0.62 (0.37, 0.93)
Perimeter	0.56 (0.46, 0.67)	0.76 (0.68, 0.84)	0.45 (0.34, 0.58)	0.47 (0.37, 0.57)
Average distance	0.66 (0.50, 0.81)	0.76 (0.68, 0.84)	0.65 (0.56, 0.74)	0.68 (0.57, 0.81)
Hausdorff distance	0.67 (0.55, 0.79)	0.75 (0.67, 0.83)	0.67 (0.62, 0.71)	0.70 (0.65, 0.75)

borders and the statistics they produce. More specifically, we can test the difference between the preedit and postedit WI values to check for a statistically significant difference. To do this, we again used a jack-knife resampling procedure to compute the 95% confidence interval of the mean difference between preedit and postedit WI values for *in vivo* luminal and medial–adventitial border detection. Mean differences based on cross-sectional area WI values and Hausdorff distance WI values are plotted in Fig. 6.

For luminal detection by the force-acceleration algorithm, there was no significant difference ($p = 0.05$) between the preedit and postedit WI values based on cross-sectional area. However, there was a significant difference for the Hausdorff distance values. For medial–adventitial border detection, both area and Hausdorff WI values show a significant difference between preedit and postedit borders. The editing improves

the results of the segmentation for the medial–adventitial border.

Comparing preedit and postedit borders using the neighborhood-search algorithm showed no significant difference ($p = 0.05$) in luminal or medial–adventitial border detection based on cross-sectional area WI values. However, for the Hausdorff WI values, there was a significant difference between preedit and postedit borders for both luminal and medial–adventitial border detection.

C. Algorithm Comparison

In addition to comparing the preedit and postedit WI values, we also gauged whether there was any significant difference, either before or after editing, between the WI values from the two algorithms. For luminal detection before editing, there was no significant difference ($p = 0.05$) between WI values for

TABLE III
WI VALUES FOR *IN VIVO* MEDIAL–ADVENTITIAL BORDER DETECTION

Parameters (3 patients, 185 images)	WI (95% Confidence intervals)			
	Force-Acceleration Algorithm		Neighborhood-Search Algorithm	
	Pre-edit	Post-edit	Pre-edit	Post-edit
Area	0.62 (0.46, 0.82)	0.77 (0.70, 0.85)	0.81 (0.72, 0.90)	0.88 (0.78, 0.97)
Perimeter	0.78 (0.76, 0.81)	0.92 (0.87, 0.96)	0.64 (0.57, 0.71)	0.71 (0.65, 0.77)
Average distance	0.63 (0.55, 0.72)	0.76 (0.72, 0.80)	0.68 (0.64, 0.71)	0.79 (0.75, 0.83)
Hausdorff distance	0.65 (0.64, 0.67)	0.77 (0.73, 0.81)	0.70 (0.67, 0.74)	0.80 (0.74, 0.86)

TABLE IV
WI VALUES FOR *IN VITRO* LUMINAL BORDER DETECTION

Parameters (3 vessels, 180 images)	WI (95% Confidence intervals)			
	Force-Acceleration Algorithm		Neighborhood-Search Algorithm	
	Pre-edit	Post-edit	Pre-edit	Post-edit
Area	0.66 (0.54, 0.79)	0.72 (0.62, 0.82)	0.87 (0.76, 0.98)	0.90 (0.78, 1.03)
Perimeter	0.83 (0.65, 1.00)	0.84 (0.68, 1.00)	0.64 (0.48, 0.81)	0.68 (0.52, 0.83)
Average distance	0.65 (0.59, 0.71)	0.71 (0.69, 0.72)	0.69 (0.62, 0.75)	0.71 (0.64, 0.79)
Hausdorff distance	0.68 (0.60, 0.75)	0.74 (0.73, 0.74)	0.69 (0.63, 0.76)	0.74 (0.67, 0.81)

TABLE V
WI VALUES FOR *IN VITRO* MEDIAL–ADVENTITIAL BORDER DETECTION

Parameters (3 vessels, 180 images)	WI (95% Confidence intervals)			
	Force-Acceleration Algorithm		Neighborhood-Search Algorithm	
	Pre-edit	Post-edit	Pre-edit	Post-edit
Area	0.52 (-0.02, 1.11)	0.58 (-0.08, 1.31)	0.61 (0.32, 0.89)	0.58 (0.20, 0.96)
Perimeter	0.88 (0.64, 1.13)	0.97 (0.82, 1.12)	0.70 (0.62, 0.78)	0.83 (0.76, 0.90)
Average distance	0.54 (0.28, 0.81)	0.62 (0.29, 0.97)	0.57 (0.51, 0.62)	0.63 (0.50, 0.75)
Hausdorff distance	0.62 (0.52, 0.72)	0.65 (0.52, 0.78)	0.66 (0.62, 0.70)	0.72 (0.69, 0.76)

cross-sectional area or Hausdorff distance, as shown in Fig. 7. However, for medial–adventitial border detection, the neighborhood-search algorithm had better results (WI closer to 1.0), as there was a significant difference between the WI values for the two techniques based on both cross-sectional area and Hausdorff distance.

After editing, there was no significant difference ($p = 0.05$) in luminal or medial–adventitial border detection for either cross-sectional area or Hausdorff distance WI values. However, we again found a significant difference in medial–adventitial border detection WI values for Hausdorff distance. The neighborhood-search technique produced WI values closer to 1.0. For cross-
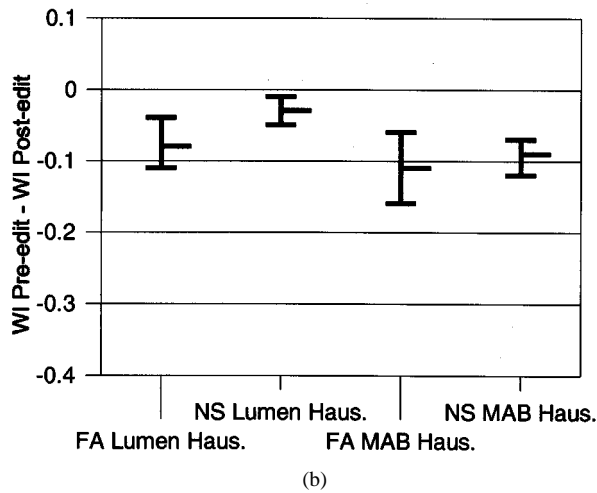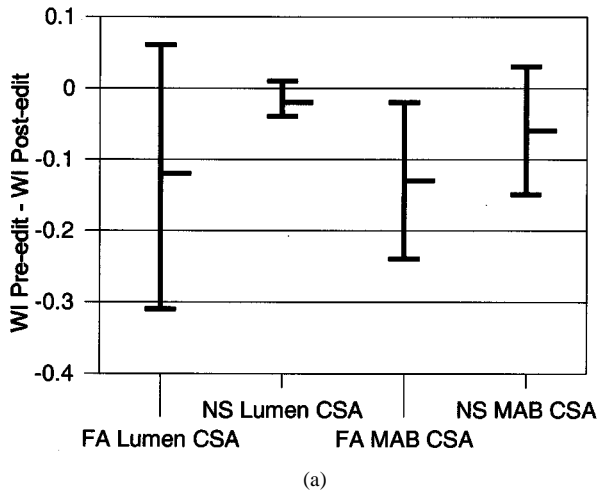
Fig. 6. Plot of the difference in WI (WI) values for detected borders before editing and the borders after editing. (a) WI value was calculated using cross-sectional area measurements. (b) Hausdorff distance was used to calculate WI. The 95% confidence intervals are shown.
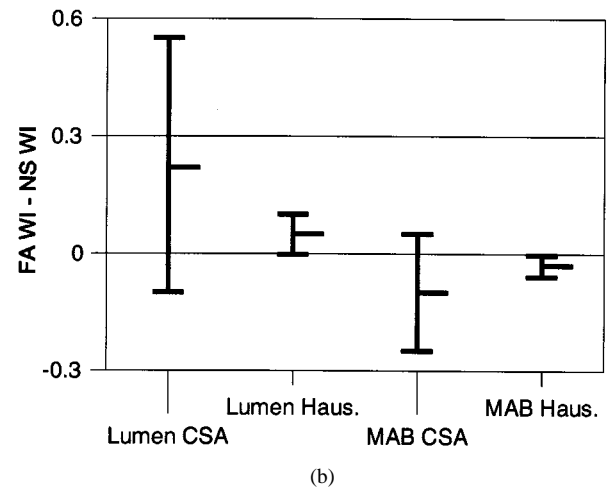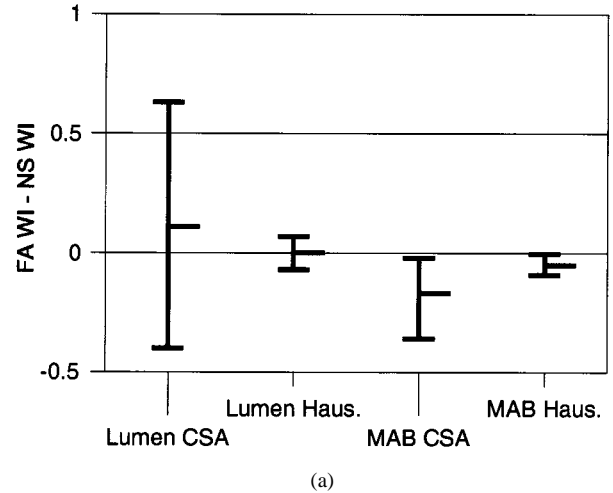
Fig. 7. Plot of the difference in WI values for detected borders from the force-acceleration algorithm and the neighborhood-search algorithm. Differences before editing are shown in (a) and differences after editing are plotted in (b). The 95% confidence intervals are shown.

sectional area, there was no difference between borders detected by the two algorithms.

D. Known-Volume Phantom

The clear acrylic phantom constructed for volume validation consisted of five different sections, each with a known volume. Precise physical measurements of the diameter and length of each section were used to calculate the volume using the equation for a cylinder. Three independent pullbacks performed with the phantom yielded 15 volumetric sections. The beginning and end could not be clearly defined for the last section of one pullback, therefore, only 14 sections were used for comparison. The volumes calculated from the IVUS images, from which the phantom borders were detected with both the force-acceleration algorithm and the neighborhood-search algorithm, were compared with the known volume of each section. The measurements from both algorithms and the actual volumes, along with percent bias are shown in Table VI for comparison.

E. Algorithm Timing

The average CPU time for preprocessing and snake deformation for both algorithms is shown in Table VII. The force-accel-

eration technique required on the order of 1 h of CPU time, while the neighborhood-search technique required approximately 1 min of CPU time, making the neighborhood-search technique approximately 60 times faster in terms of CPU time needed for both techniques.

V. DISCUSSION

For a comparison of the two techniques presented, two fundamental questions were addressed. The first is whether either of the algorithms was more accurate in the validation, and the second is whether either algorithm requires less computational expense. As presented in Fig. 7, which compares the WI values from the force-acceleration technique and the neighborhood-search technique, it was found that there was no significant difference ($p = 0.05$) in WI values for cross-sectional area. These data, along with the raw WI values shown in Tables II and III, lead us to conclude that both algorithms were robust and provided accurate results for *in vivo* luminal detection within the context of interobserver variability. The comparison of WI values based on a more stringent border measure, Hausdorff distance, revealed that for both preedit and postedit luminal borders there was no significant difference ($p = 0.05$). However, for medial–adventitial border detection,

TABLE VI
VOLUME CALCULATIONS FOR PHANTOM VALIDATION

Pull-back	Section	Diameter (mm)	Length (mm)	Actual volume (mm^3)	Computed volume (mm^3)		Bias (%)	
					Force-accel. algorithm	N'hood-search algorithm	Force-accel. algorithm	N'hood-search algorithm
1	1	2.03	10.31	33.43	32.72	32.55	-2.15	-2.65
1	2	2.97	10.28	71.27	68.76	68.25	**-3.51**	**-4.23**
1	3	3.99	9.41	117.48	123.72	120.97	5.31	**2.97**
1	4	5.21	10.00	212.94	217.95	212.62	2.35	-0.15
2	1	2.03	10.31	33.43	34.86	33.47	4.27	0.10
2	2	2.97	10.28	71.27	70.15	68.72	-1.57	-3.58
2	3	3.99	9.41	117.48	122.67	117.45	4.42	-0.03
2	4	5.21	10.00	212.94	216.51	210.01	1.67	-1.38
2	5	5.97	10.00	279.83	299.23	282.83	**6.93**	1.07
3	1	2.03	10.31	33.43	34.95	33.31	4.53	-0.37
3	2	2.97	10.28	71.27	72.16	70.36	1.25	-1.28
3	3	3.99	9.41	117.48	122.97	118.58	4.67	0.94
3	4	5.21	10.00	212.94	221.72	214.17	4.12	0.57
3	5	5.97	10.00	279.83	292.82	282.67	4.64	1.02

Maximum and minimum values are shown in bold type. For the force-acceleration algorithm, $R^2 = 0.99$ ($y = 1.06x - 2.71$), and for the neighborhood-search algorithm, $R^2 = 0.99$ ($y = 1.01x - 1.37$).

TABLE VII
CPU TIMES REQUIRED FOR ANALYSIS

Task (all times in msec - avg. $\pm$ stdev)	Force-acceleration algorithm	Neighborhood-search algorithm
Pre-processing	154 659.1 $\pm$ 1 058.0	37 565.6 $\pm$ 211.9
Snake deformation	3 254 480.5 $\pm$ 96 080.2	16 529.3 $\pm$ 250.4
Total	**3 409 129.6 $\pm$ 96 669.8**	**54 094.9 $\pm$ 394.6**

there was a difference between WI values both before and after editing. The raw WI values in Table III show that the neighborhood-search algorithm introduced less variability when both the preedit and postedit borders were compared with the borders traced by four expert observers.

Although a detailed analysis of the computational properties of the algorithms presented is beyond the scope of this study, the large disparity in CPU time could be attributed to several factors. First, the vertex locations for the force-acceleration model are calculated as real values, while the new locations for vertices in the neighborhood-search algorithm were calculated on a discrete grid. Also, the force-acceleration model required the calculation of internal force, external force (based on a lookup

into the preprocessed gradient data), and damping force for each vertex, which were then used to calculate an acceleration and a displacement for each vertex. These calculations were repeated for each iteration of the deformation. However, the neighborhood-search algorithm requires only the calculation of curvature and continuity, plus a lookup into the gradient data. These terms are then used to calculate energy, which is employed to decide the new location of the vertex. Another fundamental difference between the computation of the algorithms is the resampling procedure. The number of vertices on each contour of the force-acceleration model can change between each iteration, while the neighborhood-search algorithm begins with a fixed number of vertices for each contour and maintains the
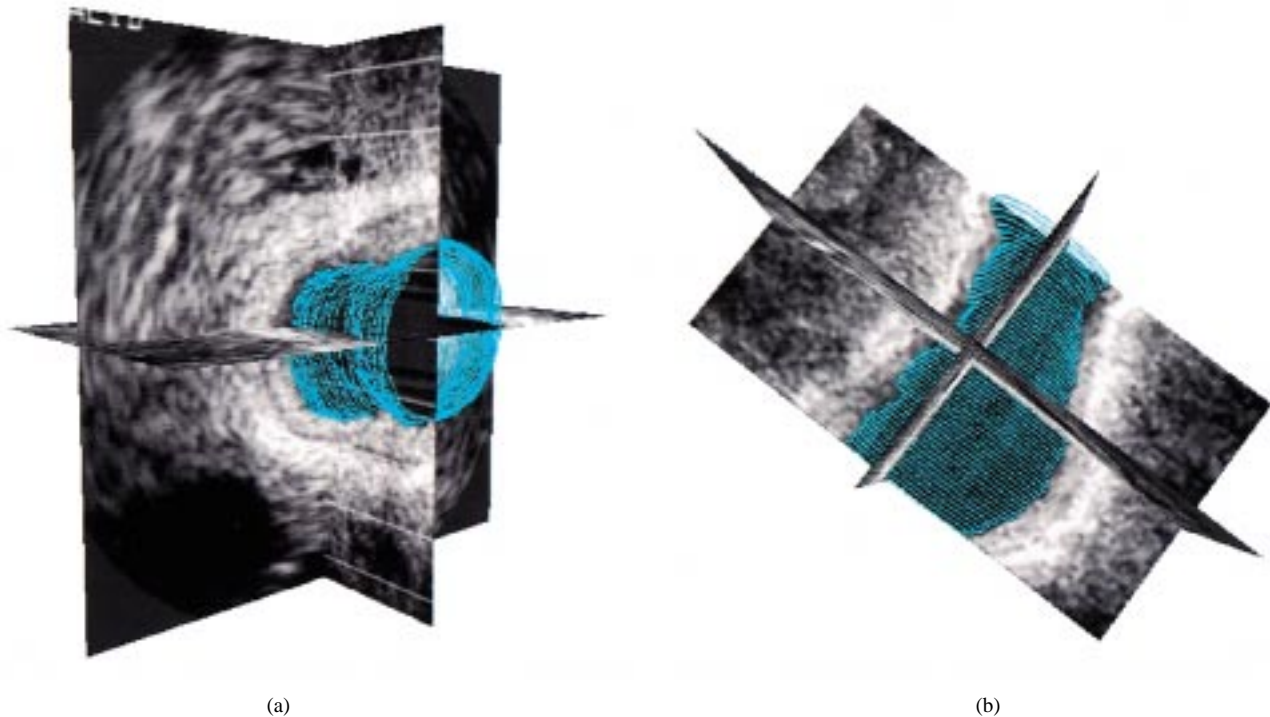
(a)   (b)

Fig. 8. 3-D rendering of detected luminal borders for an *in vitro* example. Orthogonal slices through the 3-D IVUS data set are displayed in views (a) and (b).

same number through all iterations. The computational expense of the algorithm depends on the number of vertices on each contour. As the number of vertices increases due to a vessel with large cross-sectional area, the computation time increases. For the neighborhood-search algorithm, computation time is independent of cross-sectional area, but could be higher for a larger number of initial points.

Not only did the computational complexity of the deformation algorithms affect the analysis time, but the preprocessing scheme had a significant impact as well. The 3-D gradient and Gaussian smoothing calculations performed to create the potential field for the force-acceleration algorithm were computationally intense. Different gradient schemes were informally investigated for the neighborhood-search algorithm and their effects noted. A simpler one-dimensional radial gradient scheme was chosen because it produced results which were qualitatively comparable to the more complex 3-D gradient and Gaussian smoothing computations. The simpler preprocessing scheme and the more efficient snake deformation both contributed to the fast segmentation by the neighborhood-search technique.

Our two questions, whether either algorithm is more accurate or produces results more quickly, are answered by the data presented. Comparison of WI results show that the neighborhood-search algorithm and force-acceleration model are equally accurate for luminal detection, but the neighborhood-search algorithm was slightly more accurate for medial–adventitial border detection when judged within the framework of interobserver variability.

Although the neighborhood-search algorithm provided a more computationally efficient segmentation technique than the force-acceleration algorithm, it was determined that a large component of the time required for the process was user-interaction, especially user correction of the borders after deformation. For example, a sequence of 60 IVUS images required approximately 20–25 min for analysis, including entering the initial control points, running the snake algorithm, and making corrections to the resulting borders if necessary.

A statistical comparison was also performed to assess the difference between the identified borders before the user was allowed to correct them and the borders after correction. If there is no difference between the preedit and postedit borders, then it may not be necessary to edit the borders to produce statistically accurate results, which would reduce the time needed for analysis. Cross-sectional area-based preedit border WI values and postedit border WI values for luminal and medial–adventitial border detection by the neighborhood-search algorithm are not statistically different ($p = 0.05$). However, for Hausdorff distance, there is a statistical difference ($p = 0.05$) as shown in Table V. Quantitative studies on clinical data, such as those performed by the IVUS Core Laboratory at the Cleveland Clinic Foundation [63] rely on cross-sectional area data from each image, which is used to calculate an estimate of plaque volume. Therefore, user correction of detected borders may not be necessary to accurately quantify plaque volume for studies of disease progression or regression.

Various degrees of interactivity are incorporated into IVUS image analysis techniques, placing each somewhere in the middle of the spectrum between fully automated and entirely manual approaches. The long-term goal of IVUS image analysis is certainly fully automated identification of the luminal and medial–adventitial borders. However, the challenge of developing a fully automated approach which is robust to the large degree of biological variability common in medical image anal-

ysis as well as the limitations associated with IVUS imaging is likely to sustain the importance of interactive approaches. This is even more crucial for applications, such as IVUS imaging, in which inaccurate identification of objects is unacceptable. As a result, the ease with which a user can interact with the image data and shapes modeling the anatomical structures is a critical point. In this study, manual interaction with the neighborhood-search algorithm, including entering the initial control points and making any necessary corrections to the detected borders, accounted for over 90% of the total analysis time. Therefore, if these interaction techniques could be improved and made more efficient, the time required would be reduced. The GUI designed for IVUS segmentation allows 3-D segmentation, but only provides for separate 2-D interaction with each image slice, both in placing the initial template within the data, and for user correction after the snake deformation. Three-dimensional interaction, in which the shape template could be placed in the data and corrected directly in 3-D, would improve the ergonomics of 3-D segmentation. Geometric modeling and 3-D surface warping will be investigated to aid in these 3-D interactions (see Fig. 8).

We have presented techniques which provide accurate segmentation of luminal and medial–adventitial borders from IVUS image sequences quickly. However, several limitations of the current study must be considered. Although several hundred images were analyzed for validation, they arose from only three *in vivo* cases and three *in vitro* cases. This has ramifications on the jack-knifing approach used in the statistical analysis. To calculate confidence intervals, the observations from subject 1 were discarded and WI was calculated, then the observations from the first subject were restored and observations from the next subject were discarded for the WI calculation. This is performed for n WI calculations, which are then used to calculate a standard error and a subsequent confidence interval. If each image were treated as an independent subject, we would have $n = 180$ for *in vitro* images and $n = 185$ for *in vivo* images. However, to be statistically accurate, $n = 3$ was used, which had the effect of widening the confidence intervals. Further validation using pullbacks from many more patients to increase the n would strengthen the approach, but would require manual tracing of thousands of images for WI validation.

As with many active contour based approaches, our techniques require the placement of an initial surface template, which is then deformed to make it "snap" to the feature of interest. A limitation of both the force-acceleration algorithm and the neighborhood-search algorithm is that the initial surface template must be near the edges of interest. The paradigm we used for image segmentation in which the user approximates the desired feature and then the initial template is optimized using an active contour or deformable model algorithm allows the expertise of the user to influence object detection. However, associated with this paradigm is a capture range, or a specified distance from the desired result that the initial contour must be within, in order for the initial contour to converge on the desired structure. One can think of this capture range as a function of image quality. Images with clear object boundaries have large capture ranges and those with boundaries that are indistinct or disconnected would have smaller capture ranges.

Techniques exist which can help contours or surfaces converge on structures of interest when the initial guess is farther from these desired structures. Images used to test these algorithms are usually contrived to have few gray levels and very strong, clear object boundaries. However, IVUS images have low SNR, a large degree of speckle, and are often subject to intensity dropout. The large degree of variability in atherosclerotic lesion morphometry also makes the incorporation of this feature into an IVUS segmentation algorithm difficult.

The algorithms tested in this study are also limited by their inclusion of only gradient information in the external forces. It would be possible to incorporate other features from the image data, such as texture parameters, into the external forces of these techniques, possibly making them more robust. The use of 40- and 45-MHz imaging catheters could, in principle, provide more textural information than the 20- and 30-MHz catheters reported earlier [18], [19]. However, previous experience with texture methods [15] has shown that calculating these parameters is time consuming and could make the segmentation task less efficient.

The data analyzed for the validation of the active surface segmentation algorithms was digitized from S-VHS video tape, which is also a limitation of the present study. It is well known that the digitization process can compromise the quality and resolution of IVUS data, decreasing it significantly. Our group has recently gained access to the raw ultrasound backscatter data before it is written to video. The IVUSLab software employed in this study also allows for input of this backscattered data and reconstruction and analysis of subsequent IVUS images. Eliminating the digitization step in the process will increase the resolution of the images (therefore, improving segmentation results) and also make it possible for truly on-line analysis in the catheterization laboratory, a major goal in our ongoing research.

Another limitation of the *in vivo* segmentation was the presence of the guidewire, which produced large gradient values. These large external forces pull the snake toward them. Therefore, if there was not sufficient space between the luminal border and the guidewire, the snake could converge on the inside of the guidewire and underestimate luminal area. A similar effect could occur if there were a significant ring-down artifact. If the catheter was touching the inside of the vessel wall, separation of the luminal border from the ring-down artifact was difficult and manual correction was often needed in these cases.

VI. CONCLUSION

The task of identifying luminal and medial–adventitial borders in IVUS image sequences is a challenging problem to which the application of deformable model segmentation algorithms can provide a promising solution. The manual identification of these borders, which is the current standard for quantitative analysis in trials studying atherosclerosis and the effects of drugs and other therapeutic devices on coronary artery disease, is tedious, time-consuming, and subject to large interobserver variability. A more reproducible, faster approach was presented here, which could aid in such studies.

As histology tissue preparation has been shown to shrink specimens, no true gold standard exists for comparison with algorithm results. Therefore, the techniques were assessed within the context of interobserver variability comparing them to the average of four expert human observers. WI analysis of each algorithm showed that the variability between borders from the computer and the expert observers is only slightly larger than the average variability among the observers. Both techniques produced accurate, robust results. However, the neighborhood-search algorithm required less analysis time than the force-acceleration algorithm. It can also perform as well as an expert human observer and requires a fraction of the time for analysis. More thorough clinical validation, with a large number of ECG-gated pull-back sequences, will strengthen the validity of the technique, which has substantial potential for routine clinical analysis.

REFERENCES

[1] E. Falk, P. K. Shah, and V. Fuster, "Coronary plaque disruption," *Circulation*, vol. 92, pp. 657–671, 1995.
[2] S. E. Nissen, "Shortcomings of coronary angiography and their implications in clinical practice," *Cleveland Clin. J. Med.*, vol. 66, pp. 479–485, 1999.
[3] S. E. Nissen, J. C. Gurley, C. L. Grines, D. C. Booth, R. McClure, M. Berk, C. Fischer, and A. N. DeMaria, "Intravascular ultrasound assessment of lumen size and wall morphology in normal subjects and patients with coronary artery disease," *Circulation*, vol. 84, pp. 1087–1099, 1991.
[4] J. A. Mallery, J. M. Tobis, J. Griffith, J. Gessert, M. McRae, O. Moussabeck, M. Bessen, M. Moriuchi, and W. L. Henry, "Assessment of normal and atherosclerotic arterial wall thickness with an intravascular ultrasound imaging catheter," *Amer. Heart J.*, vol. 119, pp. 1392–1400, 1990.
[5] E. J. Gussenhoven, P. A. Frietman, S. H. The, R. J. van Suylen, F. C. van Egmond, C. T. Lancee, H. van Urk, J. R. Roelandt, T. Stijnen, and N. Bom, "Assessment of medial thinning in atherosclerosis by intravascular ultrasound," *Amer. J. Cardiol.*, vol. 68, pp. 1625–1632, 1991.
[6] C. J. Davidson, K. H. Sheikh, J. K. Harrison, S. I. Himmelstein, M. E. Leithe, K. B. Kisslo, and T. M. Bashore, "Intravascular ultrasonography versus digital subtraction angiography: A human *in vivo* comparison of vessel size and morphology," *J. Amer. Coll. Cardiol.*, vol. 16, pp. 633–636, 1990.
[7] G. S. Mintz, J. A. Painter, A. D. Pichard, K. M. Kent, L. F. Satler, J. J. Popma, Y. C. Chuang, T. A. Bucher, L. E. Sokolowicz, and M. B. Leon, "Atherosclerosis in angiographically 'normal' coronary artery reference segments: An intravascular ultrasound study with clinical correlations," *J. Amer. Coll. Cardiol.*, vol. 25, pp. 1479–1485, 1995.
[8] E. M. Tuzcu, B. Berkalp, A. C. DeFranco, S. G. Ellis, M. Goormastic, P. L. Whitlow, I. Franco, R. E. Raymond, and S. E. Nissen, "The dilemma of diagnosing coronary calcification: Angiography versus intravascular ultrasound," *J. Amer. Coll. Cardiol.*, vol. 27, pp. 832–838, 1996.
[9] E. J. Topol and S. E. Nissen, "Our preoccupation with coronary luminology. The dissociation between clinical and angiographic findings in ischemic heart disease," *Circulation*, vol. 92, pp. 2333–2342, 1995.
[10] R. Blasini, F. J. Neumann, C. Schmitt, J. Bokenkamp, and A. Schomig, "Comparison of angiography and intravascular ultrasound for the assessment of lumen size after coronary stent placement: Impact of dilation pressures," *Cathet. Cardiovasc. Diagn.*, vol. 42, pp. 113–119, 1997.
[11] J. M. Hodgson, K. G. Reddy, R. Suneja, R. N. Nair, E. J. Lesnefsky, and H. M. Sheehan, "Intracoronary ultrasound imaging: Correlation of plaque morphology with angiography, clinical syndrome and procedural results in patients undergoing coronary angioplasty," *J. Amer. Coll. Cardiol.*, vol. 21, pp. 35–44, 1993.
[12] R. T. Lee, H. M. Loree, G. C. Cheng, E. H. Lieberman, N. Jaramillo, and F. J. Schoen, "Computational structural analysis based on intravascular ultrasound imaging before *in vitro* angioplasty: Prediction of plaque fracture locations," *J. Amer. Coll. Cardiol.*, vol. 21, pp. 777–782, 1993.
[13] J. M. Tobis, D. J. Mahon, S. L. Goldberg, S. Nakamura, and A. Colombo, "Lessons from intravascular ultrasonography: Observations during interventional angioplasty procedures," *J. Clin. Ultrasound*, vol. 21, pp. 589–607, 1993.
[14] M. Masseroli, R. M. Cothren, D. S. Meier, E. M. Tuzcu, D. G. Vince, S. E. Nissen, J. D. Thomas, and J. F. Cornhill, "Quantification of intramural calcification in coronary intravascular ultrasound images with automated image analysis," *Amer. Heart J.*, vol. 136, pp. 78–86, 1998.
[15] D. G. Vince, K. J. Dixon, R. M. Cothren, and J. F. Cornhill, "Comparison of texture analysis methods for the characterization of coronary plaques in intravascular ultrasound images," *Computerized Med. Imag. and Graphics*, vol. 24, pp. 221–229, 2000.
[16] D. S. Meier, R. M. Cothren, D. G. Vince, and J. F. Cornhill, "Automated morphometry of coronary arteries with digital image analysis of intravascular ultrasound," *Amer. Heart J.*, vol. 133, pp. 681–690, 1997.
[17] C. J. Bouma, W. J. Niessen, K. J. Zuiderveld, E. J. Gussenhoven, and M. A. Viergever, "Evaluation of segmentation algorithms for intravascular ultrasound images," *Visualization Biomed. Computing*, pp. 203–212, 1996.
[18] A. Mojsilovic, M. Popovic, N. Amodaj, R. Babic, and M. Ostojic, "Automatic segmentation of intravascular ultrasound images: A texture-based approach," *Ann. Biomed. Eng.*, vol. 25, pp. 1059–1071, 1997.
[19] M. Sonka, X. Zhang, M. Siebes, M. S. Bissing, S. C. DeJong, S. M. Collins, and C. R. McKay, "Segmentation of intravascular ultrasound images: A knowledge-based approach," *IEEE Trans. Med. Imag.*, vol. 14, pp. 719–732, Dec. 1995.
[20] J. Vandenberg, G. Liersch, H. Hanna, and J. Cameron, "Fully automated media and lumen boundary detection in intravascular ultrasound images," *Proc. IEEE Southwest Symp. Image Analysis and Interpretation*, pp. 71–75, 1996.
[21] R. Shekhar, R. M. Cothren, D. G. Vince, S. Chandra, J. D. Thomas, and J. F. Cornhill, "Three-dimensional segmentation of luminal and adventitial borders in serial intravascular ultrasound images," *Computerized Med. Imag. and Graphics*, vol. 23, pp. 299–309, 1999.
[22] C. von Birgelen, C. Di Mario, W. Li, J. C. Schuurbiers, C. J. Slager, P. J. de Feyter, J. R. Roelandt, and P. W. Serruys, "Morphometric analysis in three-dimensional intracoronary ultrasound: An *in vitro* and *in vivo* study performed with a novel system for the contour detection of lumen and plaque," *Amer. Heart J.*, vol. 132, pp. 516–527, 1996.
[23] W. Li, J. G. Bosch, Y. Zhong, W. J. Gussenhoven, H. Rijsterborgh, J. H. C. Reiber, and N. Bom, "Semiautomatic frame-to-frame tracking of the luminal border from intravascular ultrasound," *Comput. Cardiol*, pp. 353–356, 1992.
[24] X. Zhang, C. R. McKay, and M. Sonka, "Tissue characterization in intravascular ultrasound images," *IEEE Trans. Med. Imag.*, vol. 17, pp. 889–899, Dec. 1998.
[25] C. von Birgelen, A. van der Lugt, A. Nicosia, G. S. Mintz, E. J. Gussenhoven, E. de Vrey, M. T. Mallus, J. R. Roelandt, P. W. Serruys, and P. J. de Feyter, "Computerized assessment of coronary lumen and atherosclerotic plaque dimensions in three-dimensional intravascular ultrasound correlated with histomorphometry," *Amer. J. Cardiol.*, vol. 78, pp. 1202–1209, 1996.
[26] R. J. Frank, D. D. McPherson, K. B. Chandran, and E. L. Dove, "Optimal surface detection in intravascular ultrasound using multi-dimensional graph search," *Comput. Cardiol*, pp. 45–48, 1996.
[27] J. Hu and X. Hu, "Approach to automatic segmentation of 3-D intravascular ultrasound images," in *Proc. IEEE Nuclear Science Symp. Medical Imaging Conf.*, vol. 3, 1995, pp. 1461–1464.

[28] M. Sonka, W. Liang, X. Zhang, S. DeJong, S. M. Collins, and C. R. McKay, "Three-dimensional automated segmentation of coronary wall and plaque from intravascular ultrasound pullback sequences," *Comput. Cardiol.*, pp. 637–640, 1995.

[29] K. Rosenfield, D. W. Losordo, K. Ramaswamy, J. O. Pastore, R. E. Langevin, S. Razvi, B. D. Kosowsky, and J. M. Isner, "Three-dimensional reconstruction of human coronary and peripheral arteries from images recorded during two-dimensional intravascular ultrasound examination," *Circulation*, vol. 84, pp. 1938–1956, 1991.

[30] P. J. Dhawale, D. L. Wilson, and J. M. Hodgson, "Volumetric intracoronary ultrasound: Methods and validation," *Cathet. Cardiovasc. Diagn.*, vol. 33, pp. 296–307, 1994.

[31] ——, "Optimal data acquisition for volumetric intracoronary ultrasound," *Cathet. Cardiovasc. Diagn.*, vol. 32, pp. 288–299, 1994.

[32] P. J. Dhawale, Q. Rasheed, N. Griffin, D. L. Wilson, and J. M. Hodgson, "Intracoronary ultrasound plaque volume quantification," *Comput. Cardiol*, pp. 121–124, 1993.

[33] N. Bruining, C. von Birgelen, P. J. de Feyter, J. Ligthart, W. Li, P. W. Serruys, and J. R. Roelandt, "ECG-gated versus nongated three-dimensional intracoronary ultrasound analysis: Implications for volumetric measurements," *Cathet. Cardiovasc. Diagn.*, vol. 43, pp. 254–260, 1998.

[34] C. von Birgelen, E. A. de Vrey, G. S. Mintz, A. Nicosia, N. Bruining, W. Li, C. J. Slager, J. R. Roelandt, P. W. Serruys, and P. J. de Feyter, "ECG-gated three-dimensional intravascular ultrasound: Feasibility and reproducibility of the automated analysis of coronary lumen and atherosclerotic plaque dimensions in humans," *Circulation*, vol. 96, pp. 2944–2952, 1997.

[35] C. von Birgelen, P. J. de Feyter, E. A. de Vrey, W. Li, N. Bruining, A. Nicosia, J. R. Roelandt, and P. W. Serruys, "Simpson's rule for the volumetric ultrasound assessment of atherosclerotic coronary arteries: A study with ECG-gated three-dimensional intravascular ultrasound," *Coron. Artery Dis.*, vol. 8, pp. 363–369, 1997.

[36] F. Prati, C. Di Mario, R. Gil, C. von Birgelen, E. Camenzind, W. J. Montauban van Swijndregt, P. J. de Feyter, P. W. Serruys, and J. R. Roelandt, "Usefulness of on-line three-dimensional reconstruction of intracoronary ultrasound for guidance of stent deployment," *Amer. J. Cardiol.*, vol. 77, pp. 455–461, 1996.

[37] C. von Birgelen, G. S. Mintz, E. A. de Vrey, P. J. de Feyter, T. Kimura, J. J. Popma, M. Nobuyoshi, P. W. Serruys, and M. B. Leon, "Successful directional atherectomy of *de novo* coronary lesions assessed with three-dimensional intravascular ultrasound and angiographic follow-up," *Amer. J. Cardiol.*, vol. 80, pp. 1540–1545, 1997.

[38] E. A. de Vrey, G. S. Mintz, C. von Birgelen, T. Kimura, M. Noboyoshi, J. J. Popma, P. W. Serruys, and M. B. Leon, "Serial volumetric (three-dimensional) intravascular ultrasound analysis of restenosis after directional coronary atherectomy," *J. Amer. Coll. Cardiol.*, vol. 32, pp. 1874–1880, 1998.

[39] G. R. Dussaillant, G. S. Mintz, A. D. Pichard, K. M. Kent, L. F. Satler, J. J. Popma, and M. B. Leon, "Effect of rotational atherectomy in noncalcified atherosclerotic plaque: A volumetric intravascular ultrasound study," *J. Amer. Coll. Cardiol.*, vol. 28, pp. 856–860, 1996.

[40] C. von Birgelen, G. S. Mintz, A. Nicosia, D. P. Foley, W. J. van der Giessen, N. Bruining, S. G. Airiian, J. R. Roelandt, P. J. de Feyter, and P. W. Serruys, "Electrocardiogram-gated intravascular ultrasound image acquisition after coronary stent deployment facilitates on-line three-dimensional reconstruction and automated lumen quantification," *J. Amer. Coll. Cardiol.*, vol. 30, pp. 436–443, 1997.

[41] C. von Birgelen, M. J. Kutryk, R. Gil, Y. Ozaki, C. Di Mario, J. R. Roelandt, P. J. de Feyter, and P. W. Serruys, "Quantification of the minimal luminal cross-sectional area after coronary stenting by two- and three-dimensional intravascular ultrasound versus edge detection and videodensitometry," *Amer. J. Cardiol.*, vol. 78, pp. 520–525, 1996.

[42] M. Terashima, M. Hayakawa, K. Awano, J. Masuda, T. Mori, R. Emoto, K. Hattori, T. Inatome, and K. Maeda, "Three-dimensional reconstruction of intravascular ultrasound images of coronary stents using an ECG-gated pull-back device," *Heart Vessels*, vol. Suppl 12, pp. 188–190, 1997.

[43] A. Shiran, G. S. Mintz, B. Leiboff, K. M. Kent, A. D. Pichard, L. F. Satler, T. Kimura, M. Nobuyoshi, and M. B. Leon, "Serial volumetric intravascular ultrasound assessment of arterial remodeling in left main coronary artery disease," *Amer. J. Cardiol.*, vol. 83, pp. 1427–1432, 1999.

[44] C. von Birgelen, G. S. Mintz, E. A. de Vrey, T. Kimura, J. J. Popma, S. G. Airiian, M. B. Leon, M. Nobuyoshi, P. W. Serruys, and P. J. de Feyter, "Atherosclerotic coronary lesions with inadequate compensatory enlargement have smaller plaque and vessel volumes: Observations with three dimensional intravascular ultrasound *in vivo*," *Heart*, vol. 79, pp. 137–142, 1998.

[45] A. J. Thrush, D. E. Bonnett, M. R. Elliott, S. S. Kutob, and D. H. Evans, "Evaluation of the potential and limitations of three-dimensional reconstructions from intravascular ultrasound images," *Ultrasound Med. Biol.*, vol. 23, pp. 437–445, 1997.

[46] S. P. Wiet, M. Vonesh, M. J. Waligora, B. J. Kane, and D. D. McPherson, "Effect of vascular curvature on three-dimensional reconstruction of intravascular ultrasound images," *Ann. Biomed. Eng.*, vol. 24, pp. 695–701, 1996.

[47] A. Wahle, G. P. M. Prause, S. C. DeJong, and M. Sonka, "Geometrically correct 3-D reconstruction of intravascular ultrasound images by fusion with biplane angiography—Methods and validation," *IEEE Trans. Med. Imag.*, vol. 18, pp. 686–699, Aug. 1999.

[48] J. L. Evans, K. H. Ng, S. G. Wiet, M. J. Vonesh, W. B. Burns, M. G. Radvany, B. J. Kane, C. J. Davidson, S. I. Roth, B. L. Kramer, S. N. Meyers, and D. D. McPherson, "Accurate three-dimensional reconstruction of intravascular ultrasound data. Spatially correct three-dimensional reconstructions," *Circulation*, vol. 93, pp. 567–576, 1996.

[49] M. Laban, J. A. Oomen, C. J. Slager, J. J. Wentzel, R. Krams, J. C. H. Schuurbiers, A. den Boer, C. von Birgelen, P. W. Serruys, and P. J. de Feijter, "ANGUS: A new approach to three-dimensional reconstruction of coronary vessels by combined use of angiography and intravascular ultrasound," *Comput. Cardiol*, pp. 325–338, 1995.

[50] R. M. Cothren, R. Shekhar, E. M. Tuzcu, S. E. Nissen, J. F. Cornhill, and D. G. Vince, "Three-dimensional reconstruction of the coronary artery wall by image fusion of intravascular ultrasound and bi-plane angiography," *Proc. Int. J. Cardiac Imag.*, vol. 16, pp. 69–85, 2000.

[51] G. P. Prause, S. C. DeJong, C. R. McKay, and M. Sonka, "Accurate 3D reconstruction of tortuous coronary vessels using biplane angiography and intravascular ultrasound," *SPIE—Med. Imag.*, vol. 3033, pp. 225–234, 1997.

[52] R. Shekhar, R. M. Cothren, D. G. Vince, and J. F. Cornhill, "Fusion of intravascular ultrasound and biplane angiography for three-dimensional reconstruction of coronary arteries," *Comput. Cardiol*, pp. 5–8, 1996.

[53] J. D. Klingensmith, D. G. Vince, B. D. Kuban, R. Shekhar, E. M. Tuzcu, S. E. Nissen, and J. F. Cornhill, "Assessment of coronary compensatory enlargement by three-dimensional intravascular ultrasound," *Int. J. Cardiac Imag.*, vol. 16, pp. 87–98, 2000.

[54] J. D. Klingensmith, D. G. Vince, R. Shekhar, B. Kuban, E. M. Tuzcu, and J. F. Cornhill, "Quantification of coronary arterial plaque volume using 3D reconstructions formed by fusing intravascular ultrasound and biplane angiography," *SPIE Med. Imag.*, vol. 3660, pp. 343–350, 1999.

[55] S. Lobregt and M. A. Viergever, "Discrete dynamic contour model," *IEEE Trans. Med. Imag.*, vol. 14, pp. 12–24, Mar. 1995.

[56] D. J. Williams and M. Shah, "A fast algorithm for active contours," in *Proc. 3rd Int. Conf. Computer Vision*, 1990, pp. 592–595.

[57] ——, "A fast algorithm for active contours and curvature estimation," *CVGIP: Image Understanding*, vol. 55, pp. 14–26, 1992.

[58] M. Kass, A. Witkin, and D. Terzopoulos, "Snakes: Active contour models," in *Proc. 1st Int. Conf. Computer Vision*, 1987, pp. 259–268.

[59] V. Chalana, D. T. Linker, D. R. Haynor, and Y. Kim, "A multiple active contour model for cardiac boundary detection on echocardiographic sequences," *IEEE Trans. Med. Imag.*, vol. 15, pp. 290–298, June 1996.

[60] A. A. Amini, S. Tehrani, and T. E. Weymouth, "Using dynamic programming for minimizing the energy of active contours in the presence of hard constraints," in *Proc. 2nd Int. Conf. Computer Vision*, 1988, pp. 95–99.

[61] V. Chalana and Y. Kim, "Methodology for evaluation of boundary detection algorithms on medical images," *IEEE Trans. Med. Imag.*, vol. 16, pp. 642–652, Oct. 1997.

[62] D. P. Huttenlocher, G. A. Klanderman, and W. J. Rucklidge, "Comparing images using the Hausdorff distance," *IEEE Trans. Pattern Anal. Machine Intell.*, vol. 15, pp. 850–863, Sept. 1993.

[63] S. R. Kapadia, S. E. Nissen, K. M. Ziada, V. Guetta, T. D. Crowe, R. E. Hobbs, R. C. Starling, J. B. Young, and E. M. Tuzcu, "Development of transplantation vasculopathy and progression of donor-transmitted atherosclerosis: Comparison by serial intravascular ultrasound imaging," *Circulation*, vol. 98, pp. 2672–2678, 1998.